https://doi.org/10.5194/egusphere-2026-845
Preprint. Discussion started: 17 February 2026

In-depth characterisation of organic matter thermal lability and composition from Arctic Permafrost thaw slumps

Marco A. Bolandini[1], Jordon D. Hemingway[1], Negar Haghipour[1,2], Kirsi H. Keskitalo[4], Jorien E. Vonk[3], Timothy I. Eglinton[1], Lisa Bröder[1]

[1]Geological Institute, Department of Earth and Planetary Sciences, ETH Zurich, Sonneggstrasse 5, 8092 Zurich, Switzerland
[2]Laboratory for Ion Beam Physics, Department of Physics, ETH Zurich, Otto-Stern-Weg 5, 8093 Zurich, Switzerland
[3]Earth and Climate, Faculty of Science, Vrije Universiteit Amsterdam, De Boelelaan 1085, 1081 HV Amsterdam, Netherlands
[4]School of Geography and Natural Sciences, Northumbria University, Ellison Place, Newcastle upon Tyne UK-NE1 8ST, United Kingdom

Correspondence to: Marco A. Bolandini (marcobo@eaps.ethz.ch)

Abstract

The rapid warming of the Arctic is accelerating permafrost thaw and mobilising large, previously frozen organic-carbon reservoirs. Retrogressive thaw slumps (RTS) are dynamic hotspots of abrupt permafrost disturbance that expose deep, millennial-aged material to erosion and transport. To assess the fate of slump-derived organic matter (OM), we analysed samples from (i) the seasonally thawed active layer, (ii) Holocene and Pleistocene permafrost, (iii) freshly thawed debris, and (iv) runoff across four RTS of contrasting sizes and ecological settings on the Peel Plateau, north-western Canada. We specifically quantified OM abundance, thermal stability, and radiocarbon content, complemented by thermally-sliced pyrolysis–gas chromatography–mass spectrometry (Ts-Py-GCMS) for molecular fingerprints. Our results show that OM age and stability primarily reflect geomorphic feature type. Permafrost, debris, and runoff contain radiocarbon-depleted, thermally stable carbon, whereas active-layer OM is younger and more labile, with minor contributions of stabilised, higher-energy fractions. Ts-Py-GCMS shows that low-temperature fractions are dominated by carbohydrate- and cellulose-derived pyrolysates, while higher-temperature fractions contain aromatic and long-chain aliphatic compounds consistent with more processed or mineral-associated OM. The close similarity between permafrost, debris, and runoff indicates that RTS predominantly export ancient, thermally stable OM with limited early-stage alteration. These findings highlight that a substantial portion of thaw-mobilised particulate carbon likely remains stable during initial transport, with important implications for Arctic carbon-climate feedbacks.

https://doi.org/10.5194/egusphere-2026-845
Preprint. Discussion started: 17 February 2026

1 Introduction

Arctic amplification has led to regional warming rates two to four times the global mean (Overland et al., 2019; Rantanen et al., 2022), thus accelerating permafrost thaw and the release of large, previously frozen organic carbon stocks (Hugelius et al., 2014; Schuur et al., 2015). Soils across the permafrost region store approximately 1,000 Pg C within the upper 3 m (Hugelius et al., 2014; Mishra et al., 2021), representing nearly half of the global below-ground carbon pool. Even partial decomposition of this reservoir could substantially alter global biogeochemical cycles. Thaw and mobilisation heighten the vulnerability of this pool to decomposition, emphasising its potential role in amplifying climate warming (Schuur et al., 2015). Once thawed, some fraction of organic matter (OM) is likely remineralised, thereby leading to carbon dioxide (CO_2) and methane (CH_4) emissions and reinforcing warming (Schuur et al., 2008). However, increased plant productivity ("Arctic greening") has the potential to offset part of these emissions; the net carbon balance of the Arctic under continued warming thus remains uncertain (Strauss et al., 2025).

Retrogressive thaw slumps (RTS) are among the most dynamic features of permafrost degradation. They form when ground-ice melt triggers large-scale collapse of previously frozen deposits, exposing deep, often Pleistocene-aged material to erosion and rapid transport (French, 2007). Each slump is characterised by a steep, ice-rich headwall that retreats upslope as thaw progresses, and a downslope scar zone where thawed sediment accumulates and may be re-mobilised and transported farther downslope (Bröder et al., 2021; French, 2007; Kokelj et al., 2021; Segal et al., 2016a). Compared to gradual thaw, RTS activity strongly enhances particulate organic carbon (POC) and sediment fluxes to downstream systems (Kokelj et al., 2013, 2021; Zolkos et al., 2019). Mobilised OM can also enter river networks as dissolved organic carbon (DOC), which has been described as microbially labile (Drake et al., 2015; Mann et al., 2015; Vonk et al., 2015), while POC lability remains relatively poorly constrained. In incubation experiments this POC has shown low biodegradability (Kokelj et al., 2021), suggesting persistence after thawing. While incubation experiments provide valuable constraints on microbial respiration in thawed soils, they are usually laborious and time consuming, often underestimate the stability of mineral-associated or physically protected carbon pools and cannot resolve how molecular composition relates to OM reactivity (Lacelle et al., 2019; Shakil et al., 2022). These limitations highlight the need for complementary, process-based approaches that link OM composition to its thermal reactivity and radiocarbon-based age structure, providing mechanistic constraints on the stability and fate of RTS-derived organic carbon.

The Peel Plateau in north-western Canada is one of the most active and rapidly evolving regions of RTS development in the Arctic (Kokelj et al., 2015, 2021; Littlefair et al., 2017). Successive investigations have documented RTS-driven transformations in sediment delivery, stream geomorphology, and carbon export (Kokelj et al., 2013, 2015, 2017, 2021). These studies show that slump activity markedly increases sediment and POC fluxes, largely sourced from ancient, Holocene- and Pleistocene-aged permafrost (Bröder et al., 2021; Kokelj et al., 2021; Shakil et al., 2020; Keskitalo et al., 2021). Active-layer deepening and cryoturbation—i.e., frost-driven mixing of soil horizons and OM—further redistribute carbon vertically within thawing terrains, influencing its exposure and preservation (Bockheim and Tarnocai, 1998; Ping et al., 1998, 2008). Mapping

https://doi.org/10.5194/egusphere-2026-845
Preprint. Discussion started: 17 February 2026

and geomorphic classification efforts have demonstrated that slump morphology controls both the rate and pathway of material transfer to aquatic systems (Kokelj et al., 2013, 2015; Lewkowicz and Way, 2019; Ramage et al., 2017). Prior work on the Peel Plateau has quantified sediment and carbon fluxes and source contributions (Littlefair et al., 2017; Shakil et al., 2020; Zolkos et al., 2018) and has identified geomorphic controls on material export (Kokelj et al., 2013, 2021). Furthermore, Bröder et al. (2021) showed that active-layer material is dominated by compounds indicative of fresh plant material, whereas recently thawed debris and slump runoff predominantly carry radiocarbon-depleted POC, compositionally more similar to permafrost OM. Despite these advances, the overall assessment of bulk OM stability in these RTS systems remain poorly constrained. Specifically, how OM composition relates to its (thermal) reactivity and inferred persistence during downstream transport is not yet understood.

Here, we address these knowledge gaps by providing a mechanistic framework to distinguish stabilised versus degradable carbon fractions and assess the initial fate of slump-derived OM upon thaw and mobilisation. To do so, we collected samples at four RTS sites—spanning from small, tundra-dominated slumps to larger, forested slumps—that differed in headwall height, scar zone extent, initiation age, elevation, and predominant vegetation (Fig. 1), to measure thermal reactivity and thermally-resolved radiocarbon content together with molecular composition distributions of OM. Although thermal reactivity does not equate with bioavailability, it provides an indirect measure of OM persistence by constraining its activation energy structure (Hemingway et al., 2017). We focus on four RTS components representing two primary OM sources—the seasonally thawed active layer, and permafrost layers that formed during Holocene and Pleistocene, now exposed at the retreating headwalls—and two stages of mobilisation— freshly thawed debris accumulating at the base of the headwall and suspended sediments in runoff draining the slump scar zone. We can thus test the following hypotheses: (i) permafrost OM contains radiocarbon-depleted yet thermally heterogeneous carbon, comprising components with contrasting activation energies whose preservation reflects prolonged freezing rather than intrinsic molecular resistance. And: (ii) in contrast, the active layer contains younger organic compounds from recent biological production characterised by lower activation energies. Building on this foundation, we propose that activation-energy distributions provide a mechanistic insight into these compositional contrasts, allowing us to assess how OM from contrasting sources transforms upon erosion and transport. This information improves our understanding of how abrupt permafrost thaw and subsequent OM mobilisation influences permafrost carbon cycling and associated climate feedbacks.

2 Material and Methods

2.1 Site description and sample preparation

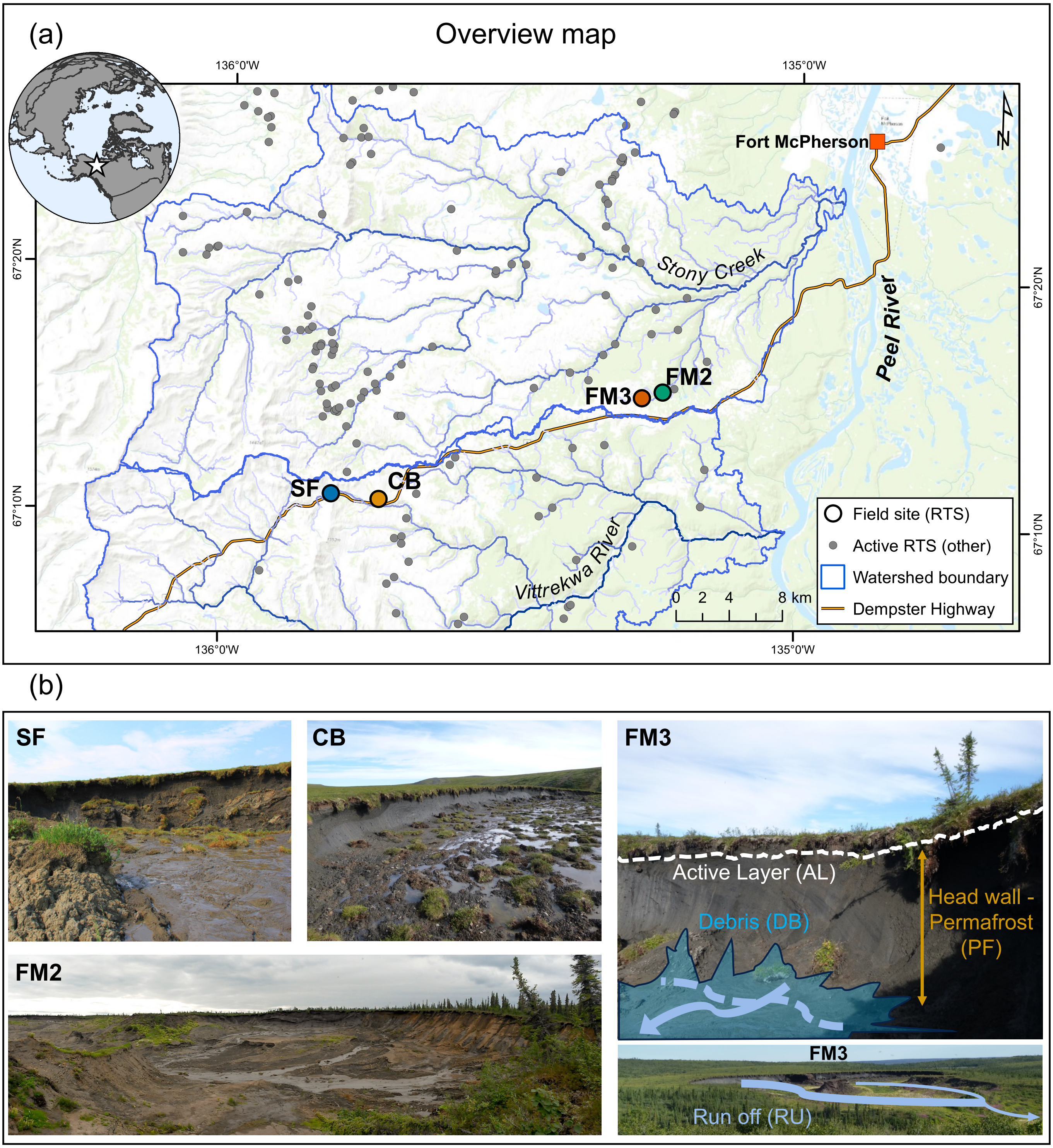

https://doi.org/10.5194/egusphere-2026-845
Preprint. Discussion started: 17 February 2026

Figure 1. (a) Map of the study area on the Peel Plateau, NWT, Canada (as indicated by the star on the inserted overview map), showing the locations of the four investigated retrogressive thaw slumps (RTS): CB (blue), SF (yellow), FM2 (green) and FM3 (red). The broader distribution of active thaw slumps across the region, mapped using Landsat imagery up to 2015, is shown as grey dots, and the Stony Creek and Vittrekwa River watersheds are outlined in blue. Geospatial data on thaw slump distribution were obtained from Segal et al. (2016). (b) Photographs of each of the RTS features. The photos of FM3 thaw slump illustrate the geomorphological features: active layer (AL – white dotted line), permafrost (PF – orange), debris (DB – blue), and runoff (RU – blue arrow). The figure has been adapted from Bröder et al. (2021) and the basemap is from Zolkos et al. (2018). Reproduced with permission from John Wiley & Sons. ©2018 American Geophysical Union.

The RTS sites studied here (Fig. 1a) have been described in detail previously (Bröder et al., 2021, Keskitalo et al., 2021) and have featured in related work on sediment dynamics and carbon fluxes (Littlefair et al., 2017; Shakil et al., 2020; Thomas et al., 2023; Zolkos et al., 2019). Sites CB and SF are smaller, more recently initiated RTS systems at higher elevation within tundra-like vegetation, whereas sites FM2 and FM3 are older, much larger and at lower elevation in more forested settings (Table 1). Samples were collected from the four key geomorphological features common to each slump: seasonally thawed active layer (AL), Holocene (HO) (and deeper Pleistocene (PL) where exposed) permafrost (PF) layers, freshly thawed slump debris (DB), and suspended sediments in runoff (RU). These zones are illustrated in the images of the FM3 headwall in Fig. 1b.

Table 1: Geomorphic characteristics of the four retrogressive thaw slumps studied. Values are based on field measurements from the 2017 campaign; further site descriptions are provided in Bröder et al. (2021), Segal et al. (2016), and Zolkos et al. (2019).

Site	**Coordinates**	**Elevation (m)**	**Active-layer depth (cm)**	**Headwall height (m)**	**Scar-zone area (ha)**
CB	67.182° N, 135.732° W	576	45–55	5–8	< 3
SF	67.183° N, 135.811° W	720	45–55	5–8	< 3
FM2	67.257° N, 135.236° W	338	20–65	up to 24	10–48
FM3	67.253° N, 135.273° W	391	20–65	up to 24	10–48

Site parameters were measured during the sampling campaign in 2017 and are described in more detail by Bröder et al. (2021) and Zolkos et al. (2019) (Table 1). In short, active-layer material was sampled from shallow soil pits, permafrost blocks were cut directly from exposed headwalls, and debris and runoff sediments were collected with stainless-steel scoops following the procedures outlined in Bröder et al. (2021). Samples were placed in pre-cleaned containers, stored frozen until return to the laboratory, and subsequently freeze-dried, ground, and homogenised prior to analysis. Inorganic carbon was removed by acid fumigation with concentrated hydrochloric acid (HCl) for 72 h at 60 °C, following standard procedures for solid-phase organic-matter analysis (Harris et al., 2001; Komada et al., 2008). Pre-treated samples from all four sites (CB, SF,

https://doi.org/10.5194/egusphere-2026-845
Preprint. Discussion started: 17 February 2026

FM2, FM3) were first analysed using solid total organic carbon analysis (SoliTOC) to provide a bulk assessment of OM content and thermal lability. A subset of samples from the larger slumps (FM2 and FM3) was subsequently investigated by online ramped oxidation-accelerator mass spectrometry (ORO-AMS) and thermally sliced-pyrolysis-gas chromatography mass spectrometry (Ts-Py-GCMS) to determine the radiocarbon age, energy distribution, and molecular composition of thermally resolved fractions.

2.2 Solid Total Organic Carbon analysis (SoliTOC)

SoliTOC analyses were carried out to obtain an overall characterisation of OM thermal stability across the geomorphological features of each thaw slump. For each sample, ~50 mg of pre-treated material was loaded into a ceramic crucible and analysed using a SoliTOC Cube analyser (Elementar GmbH) following the German industrial standard DIN 19539 (Deutsches Institut für Normung, 2016-08). Instrument calibration employed a calcium-carbonate ($CaCO_3$) standard containing 12 % total inorganic carbon (minimum p.A. quality) mixed with aluminium oxide (Al_2O_3). Analytical accuracy was verified using two certified reference materials: a high-organic-carbon sediment (Säntis SA33802151, 7.45 % C) and a low-organic-carbon soil (Säntis SA33802152, 1.54 % C). Precision within the analytical sequence was assessed using repeated analyses (n = 5 for each standard), yielded standard deviations of 0.05 % C and 0.02 % C, corresponding to relative standard deviations of 0.7 % and 1.3 %, respectively. Mean recoveries were 97.35 % (SA33802151) and 99.51 % (SA33802152), confirming stable and accurate instrument performance.

Organic carbon was quantified using three operationally defined temperature steps following DIN 19539: total organic carbon released during the 400 °C isothermal step (TOC_{400}), representing a thermally labile pool; residual oxidisable carbon (ROC), released during the subsequent 600 °C step; and total inorganic carbon (TIC), released during the final 900 °C step. Rapid heating between steps minimises CO_2 release during temperature ramps, such that carbon is operationally assigned to the target isothermal intervals rather than to a continuous temperature ramp.

The sum of TOC_{400} and ROC was defined as total organic carbon (TOC). Because a small fraction of thermally recalcitrant OC appears to combust within the nominal TIC window, the operational fractions TOC_{400} and ROC should be interpreted strictly as method-defined thermal lability pools. The ROC/TOC ratio therefore may serve as a proxy for intrinsic recalcitrance but is not necessarily identical to biological lability (see Results and Discussion for an assessment of methodological limitations). For completeness, total carbon (TC), defined as the sum of TOC and TIC, was also reported to verify bulk carbon consistency across analytical methods (Supplementary Table S2).

https://doi.org/10.5194/egusphere-2026-845
Preprint. Discussion started: 17 February 2026

2.3 Online ramped oxidation-accelerator mass spectrometry (ORO-AMS)

To resolve the age structure of OM thermal-lability fractions, ORO-AMS analyses were conducted using the setup described by Bolandini et al. (2025). This method captures and measures radiocarbon activity of CO_2 that is released across a series of temperature windows. Briefly, the system features a dual-oven configuration: the first oven (where the sample is loaded) applies a linear temperature ramp to progressively oxidise OM from the sample. Released CO_2 within each temperature window is then purified, trapped using a dual trap molecular zeolite interface (De Maria et al., 2021), it is first purified, and transferred to an accelerator mass spectrometer (Low Energy Accelerator, LEA, IonPlus) for radiocarbon measurement (Ramsperger et al., 2024; Synal et al., 2007).

In this study, approximately 40–50 mg of acid-fumigated, homogenised material from each geomorphological feature of the larger thaw slumps (FM2 and FM3) was analysed individually, including replicate combustions of selected samples (10 primary analyses plus 3 replicates). Additional combustions from FM2, FM3, CB, and SF were conducted for pre-screening and bulk characterisation. In total, more than 30 ORO combustions were performed across all sites. Samples were loaded into pre-combusted quartz tubes placed within the oxidation reactor. The ramping furnace was programmed to heat linearly at 5 °C min^{-1} from 150 °C to 900 °C under a continuous flow of 18 % O_2 in He (90 mL min^{-1}). Radiocarbon analyses were performed on predefined temperature windows (150–240, 240–300, 300–350, 350–400, 400–455, 455–510, and 510–600 °C), chosen to align with and extend the decomposition framework established by the SoliTOC analysis. For consistency, we also calculated an ORO-based ROC/TOC ratio by integrating CO_2 released between 400 and 600 °C relative to the total OC released below 600 °C. Temperatures above 600 °C were excluded from radiocarbon analysis because CO_2 yields were insufficient to sustain a stable AMS ion current and because our focus was on the sub-600 °C domain that corresponds to the operational ROC threshold used in SoliTOC. However, small amounts of refractory OC may combust above 600 °C in some samples (see Results and Discussion for an assessment of methodological limitations).

Evolved CO_2 was continuously monitored and recorded as thermograms—i.e., plots of CO_2 yield as a function of temperature—providing real-time information on OM oxidation behaviour and decomposition kinetics. Gaussian and Savitzky–Golay smoothing were applied to minimise CO_2 and temperature instrumental noise. Radiocarbon results were normalised to Ox-II reference material and corrected for machine and procedural blanks following standard ETH protocols (Synal et al., 2007) and are reported as fraction modern ($F^{14}C$), following the guidelines detailed by Reimer et al. (2004, 2020). Typical analytical uncertainties ranged from ±0.003 to ±0.010 $F^{14}C$ depending on CO_2 yield (Stuiver and Polach, 1977). For quality control, bulk-equivalent $F^{14}C$ was reconstructed as the CO_2-weighted mean of $F^{14}C$ results for each ORO-AMS thermal window and compared to previously published bulk radiocarbon measurements (Supplementary Discussion Table S1, Fig. S1, Table S3 from Bröder et al., 2021).

Subsequent data analysis integrating CO_2 thermograms with $F^{14}C$ results was performed using the open-source Python package “rampedpyrox” (Hemingway, 2016). Interpretation followed the mechanistic framework of Hemingway et al. (2017, 2019), which links decomposition profiles to underlying distributions of OM activation energy, *E*. These distributions, termed

https://doi.org/10.5194/egusphere-2026-845
Preprint. Discussion started: 17 February 2026

p(0, *E*), represent the resistance of OM to oxidative decomposition and thus provide an integrated measure of OM reactivity governed by molecular composition and stabilisation mechanisms. To further compare *p*(0, *E*) distributions across samples, three metrics were extracted: the mean activation energy, μ_E, the standard deviation of activation energy, σ_E, and the activation energy at which CO_2 release reaches its peak, E_{max}.

2.4 Thermally sliced pyrolysis-gas chromatography-mass spectrometry (Ts-Py-GCMS)

Ts-Py-GCMS generates molecular fingerprints by thermally decomposing (in the absence of oxygen) non-volatile OM into volatile compounds, which are then separated by gas chromatography and identified via mass spectrometry based on molecular weight and fragmentation patterns (Derenne and Quéné, 2015; De Leeuw and Largeau, 1993; Lewis, 1993). Unlike more conventional flash pyrolysis methods, which generate a molecular fingerprint for one specific temperature (e.g., Kaal et al., 2009; Tolu et al., 2015), the Ts-Py-GCMS approach used here applies the same step-wise temperature windows as the ORO–AMS method. As for ORO-AMS, seven windows between 150 and 600 °C were analysed (150–240, 240–300, 300–350, 350–400, 400–455, 455–510, and 510–600 °C), together with an additional high-temperature window (600–850 °C) to capture the most thermally resistant components. No measurable carbon was detected below 150 °C.

Analyses were performed using an Agilent 7890A gas chromatograph (GC) coupled via a heated transfer line to a time-of-flight mass spectrometer (BenchTOF, Markes International). The GC was equipped with a Gerstel thermal desorption unit (TDU) pyrolysis system (Gerstel) connected to a cooled injection system (CIS), with a liquid nitrogen cryotrap for compound focusing (Gerstel). The pyrolysis unit operated in evolved gas analysis (EGA) mode with a heating rate of 1 °C s^{-1} and a maximum temperature of 850 °C. The CIS was initially cooled to −150 °C to trap the volatiles, followed by a fast-heating ramp to 320 °C with a 1-minute equilibration time, while the GC inlet temperature was maintained at 300 °C. Chromatographic separation was carried out using a DB5-ms column (30 m × 0.25 mm × 0.25 µm). The GC oven programme consisted of a 5-minute isothermal hold at 40 °C, followed by a ramp of 5 °C per minute to 270 °C, then 10 °C per minute to 320 °C with a final 10-minute hold. Each run lasted a total of 66 minutes.

Mass spectra were acquired using the BenchTOF instrument operating with an ionisation energy of 70 eV. The transfer line was maintained at 310 °C, and the ion source at 300 °C. The instrument scanned over an m/z range of 50 to 700 with a time-of-flight resolution better than 7,000 (full width at half maximum, FWHM) and mass accuracy within ±0.1 Da. Mass spectrometry data were processed using the OpenChrom software (Wenig and Odermatt, 2010), with compound identification aided by matching against the NIST23 Mass Spectral Library. Spectral matches were only considered valid when their match factor exceeded a reliability threshold of 70%, a commonly accepted cutoff for tentative identification (Bravo et al., 2017; Tolu et al., 2015). Compound identification and classification followed the approach described by Bravo et al. (2017) and Tolu et al. (2015), integrating match quality, literature-based retention-time patterns, and biomarker grouping to assign peaks to major OM compound classes.

Compound classes identified in this study include branched/cyclic lipids (as markers of microbial origin or thermally altered OM) and *n*-alkyl lipids (straight-chain alkanes and alkenes derived from aliphatic biopolymers or thermally transformed OM). Lignin derivatives were used as biomarkers of vascular plant-derived OM (Kaal et al., 2016; Tolu et al., 2015). Pyrolysis products of carbohydrates and carbohydrate–cellulose derivatives (e.g., levoglucosan and furfural) were used to represent fresh biological inputs from plants or microbial exudates (Derenne and Quéné, 2015; Schnitzer and Monreal, 2011). Aromatic compounds, including phenols and polycyclic aromatic hydrocarbons (PAHs), derive from thermally stable precursor molecules that can form through microbial degradation, combustion, or advanced diagenesis and may also indicate mineral stabilisation of OM (Bravo et al., 2017; Kaal et al., 2009). Finally, N-containing compounds represent nitrogen-bearing molecules originating from microbial biomass, degraded proteinaceous material, or nitrogen-rich polymers such as chitin or peptidoglycans (Derenne and Quéné, 2015; Schnitzer and Monreal, 2011).

3 Results

3.1 OM thermal stability across thaw slump features

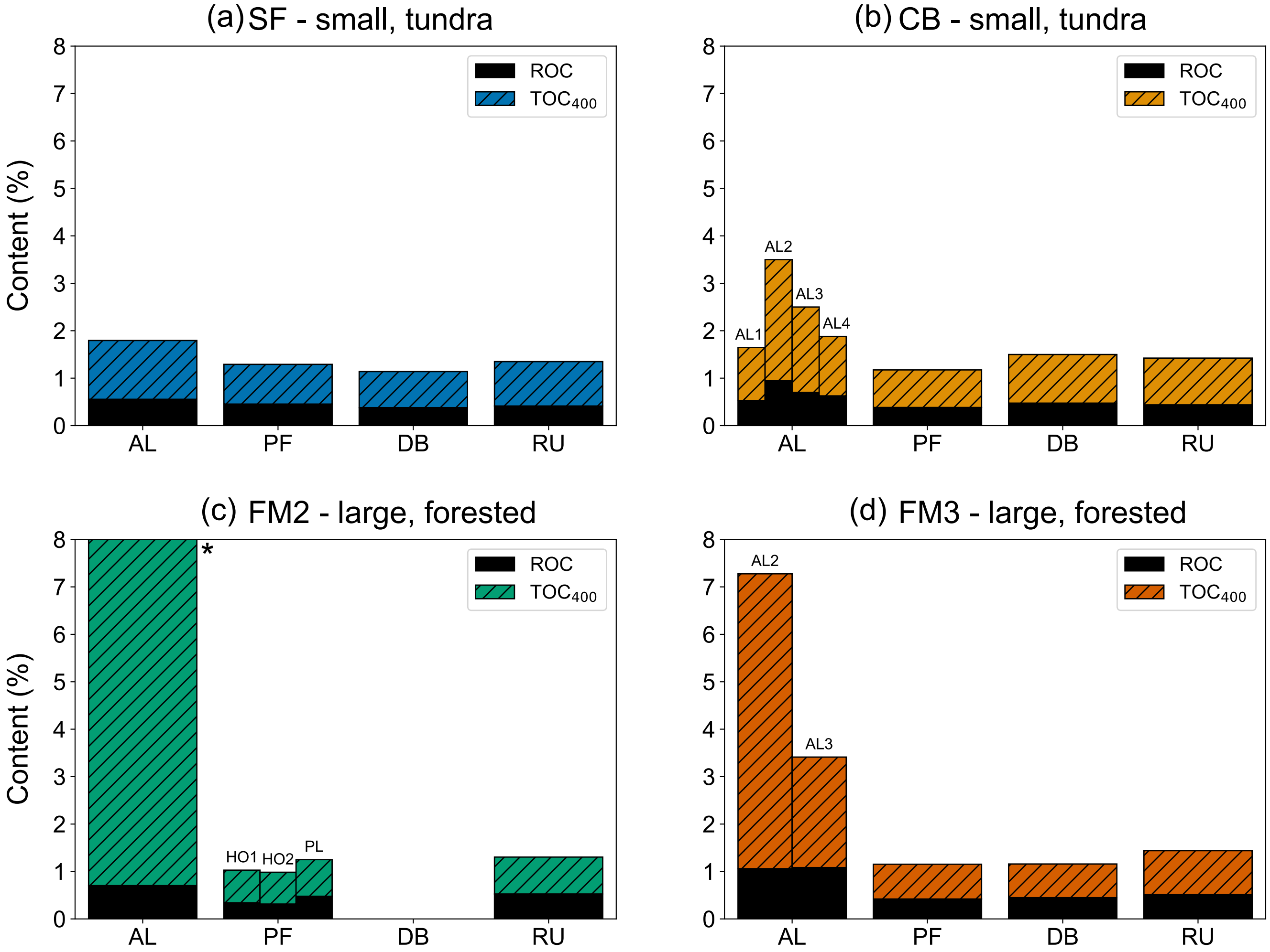

Figure 2. Carbon content in thaw slump samples as measured by Solid total organic carbon (SoliTOC) analysis. Bars represent thermally labile organic carbon (TOC_{400}; coloured) stacked above residual organic carbon (ROC; black), expressed as percent (%) of C content. Each panel (a–d) corresponds to one thaw slump site—SF (blue), CB (yellow), FM2 (green), and FM3 (red)—with bars grouped by geomorphological feature: active layer (AL), permafrost (PF), debris (DB), and runoff (RU). For FM2, both Holocene and Pleistocene permafrost layers were accessible in the field and are shown separately. Where multiple samples were collected from the same feature, individual sample names are indicated above each bar.

**The active layer sample from FM2 exhibited exceptionally high TOC_{400} content (>15%), far exceeding values measured in other geomorphological units or sites, and contributing to a combined TOC_{400} + ROC content of approximately 16%.*

Across all four slumps, the DB, RU, and PF features exhibit relatively consistent TOC_{400} and ROC contents, with TOC_{400} generally between 1.1 and 1.3 %, and ROC between 0.5 and 0.8 % (Fig. 2). By contrast, the AL shows much greater variability across sites. In the smaller slumps (CB and SF), AL samples display TOC_{400} values around 1.5 % and ROC near 1.2 %, slightly higher than in the other features of those RTS. In the larger slumps (FM2 and FM3), however, AL TOC_{400} concentrations are markedly higher, ranging from 5 % to over 16 %, while ROC remains between 0.9 and 1.4 %.

The two largest slumps, FM2 and FM3, were selected for thermally sliced radiocarbon and chemical-fingerprint analysis because their well-developed geomorphic features (distinct AL, PF, DB, and RU zones) provide the most representative and internally consistent record of thaw-slump evolution across the Peel Plateau. Normalised CO_2 thermograms reveal distinct differences in thermal behaviour across geomorphic features and sites (Fig. 3a,c). Again, AL samples show the most pronounced contrasts. In both FM2 and FM3, CO_2 release begins early—between 170 and 200 °C—and peaks sharply at relatively low temperatures. The FM2 AL sample exhibits a dominant peak near 370 °C with a shoulder plateauing at ~400 °C, while FM3 AL2 and AL3 display bimodal structures: AL2 peaks at ~300 °C and ~450 °C, and AL3 at ~300 °C with a smaller secondary peak near 450 °C. These patterns correspond to comparatively low activation energies (FM2 AL: $\mu_E = 152$ kJ mol^{-1}, $E_{\max} = 159$ kJ mol^{-1}; FM3 AL2/AL3: $\mu_E = 152$–156 kJ mol^{-1}, $E_{\max} = 140$–173 kJ mol^{-1}). Activation-energy distributions are broader in AL samples ($\mu_E \approx 21$–24 kJ mol^{-1}) than in PF-derived units, which show similarly elevated but more consolidated distributions ($\sigma_E \approx 17$–24 kJ mol^{-1}).

In both slumps, PF samples (FM2 HO1, HO2, PL; FM3 HO) display broad, asymmetric peaks. CO_2 release begins gradually near 250 °C, peaks between 370 and 400 °C, and often shows a secondary shoulder near 470 °C with extended high-temperature tails. These features align with consistently higher activation energies than in AL samples ($\mu_E \approx 162$–171 kJ mol^{-1}; $E_{\max} \approx 155$–161 kJ mol^{-1}). DB and RU samples follow similar trends to their corresponding PF layers. In FM3, both DB and RU thermograms closely resemble the HO profile and show similarly elevated activation-energy metrics ($\mu_E \approx 163$–169 kJ mol^{-1}; $E_{\max} \approx 155$–161 kJ mol^{-1}). The FM3 RU sample exhibits an earlier onset of CO_2 release (~230 °C), with peaks between ~330 and 380 °C and a secondary shoulder near 450 °C. The FM2 RU sample departs slightly from this pattern, with a peak centred near 370 °C and a pronounced shoulder around 450 °C, accompanied by activation-energy values comparable to PF ($\mu_E \approx 167$ kJ mol^{-1}; $E_{\max} \approx 157$ kJ mol^{-1}).

SoliTOC- and ORO–AMS–derived ROC/TOC ratios show consistent feature-level patterns, with higher values in PF, DB, and RU (ROC/TOC ≈ 0.25–0.45) and substantially lower values in AL (ROC/TOC typically <0.15), despite systematically lower absolute ROC/TOC values reported by ORO–AMS (Fig. S2). Method-comparison analyses show that ROC/TOC patterns are robust across SoliTOC and ORO–AMS, whereas TIC-related metrics are method-dependent and therefore not used for interpretation; full details are provided in the Supplementary Material (Figs. S2–S4; Tables S2–S3).

260 ## 3.2 Thermally-resolved radiocarbon signatures

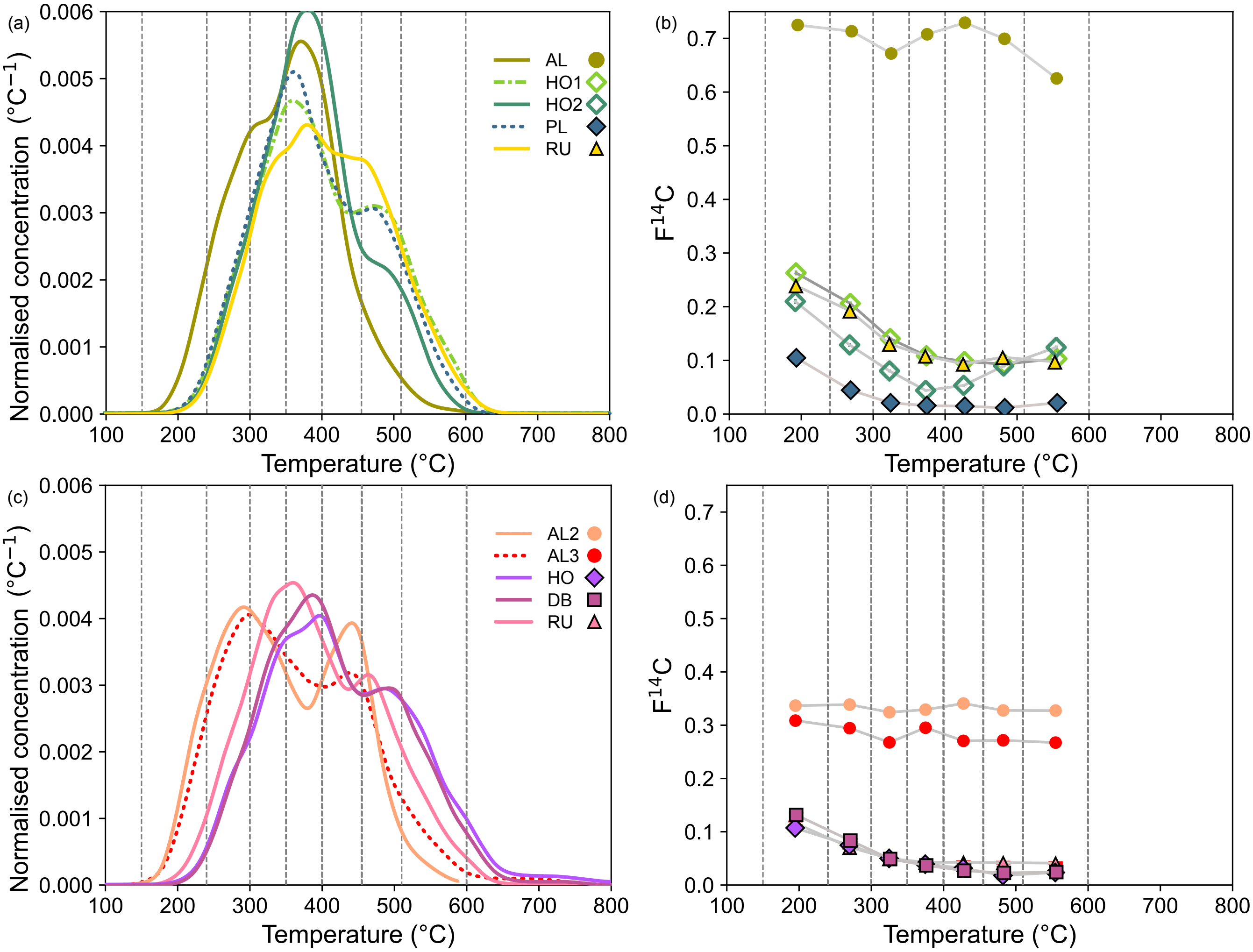

Figure 3. Panels (a) and (c): Thermograms showing the concentration of CO_2 (as area normalized concetration per °C) as a function of temperature during progressive thermal oxidation of samples from thaw slumps FM2 (a) and FM3 (c). Colours indicate feature type: active layer (AL), debris (DB), runoff (RU), and permafrost (PF), including Holocene (HO) and Pleistocene (PL) samples and line styles distinguish samples with the same geomorphological feature. All thermograms are normalised to the same integrated area, following the method of Hemingway et al. (2017). (b) and (d) Radiocarbon content ($F^{14}C$) measured across thermal decomposition windows for FM2 (b) and FM3 (d). Symbol shapes represent geomorphological features: circle = AL, square = DB, triangle = RU, diamond = PF (for FM2 - open = HO; filled = PL) and measurement uncertainties are too small to be displayed. 265

https://doi.org/10.5194/egusphere-2026-845
Preprint. Discussion started: 17 February 2026

Radiocarbon age distributions across the thermal lability spectrum were analysed for a subset of samples from the two largest slumps, FM2 and FM3 (Fig. 3b,d; Figs. S5-S14; Table S3). The FM2 AL exhibits a modest decline in $F^{14}C$ values with increasing temperature from 0.725 ± 0.008 at 150–240 °C to 0.625 ± 0.007 at 510–600 °C. (Fig. 3b). A minor decrease also occurs at 300–350 °C (0.672 ± 0.008), followed by the highest $F^{14}C$ at 400–455 °C (0.729 ± 0.008) and a gradual decline at higher temperatures. By contrast, AL samples from FM3 (Fig. 3d) show consistently lower $F^{14}C$ values. FM3 AL2 remains relatively stable, ranging from 0.337 ± 0.005 at 150–240 °C to 0.327 ± 0.006 at 510–600 °C, while AL3 is even more ^{14}C-depleted, ranging from 0.309 ± 0.006 to 0.267 ± 0.007, with no significant trend over the thermal range.

Across PF, DB, and RU, $F^{14}C$ generally decreases with increasing temperature (Fig. 3b,d). The trend is clearest in PF samples; e.g., in FM2 (Fig. 3b), HO1 $F^{14}C$ values decrease from 0.262 ± 0.005 to 0.102 ± 0.004, HO2 from 0.209 ± 0.005 to 0.123 ± 0.004, and the PL layer reaches 0.015–0.021 in the highest temperature windows, indicating near-radiocarbon-free material. Interestingly, the FM2 HO2 profile shows a partial reversal, with $F^{14}C$ reaching a minimum at 350–400 °C (0.042 ± 0.002) before rising to 0.123 ± 0.004 at 510–600 °C. FM3 HO (Fig. 3d) exhibits a similar depletion trend, decreasing from 0.106 ± 0.004 to 0.023 ± 0.002, with a signal near radiocarbon-dead for the highest temperature window.

In FM2, the RU sample exhibits a pronounced decline in $F^{14}C$ from 0.239 ± 0.006 to 0.097 ± 0.003 across the thermal windows, a pattern closely resembling the behaviour of the HO1 layer rather than the deeper PL PF. In FM3, both DB and RU decrease from initial values of ~0.13 and ~0.12 to 0.025 and 0.041, respectively, at 510–600 °C, which is almost identical to HO PF. Together, these patterns show that $F^{14}C$ systematically decreases with thermal resistance across all features except the AL. Finally, weighted-average bulk $F^{14}C$ reconstructed from all ORO–AMS thermal windows closely match independent EA–AMS bulk measurements (Fig. S1; $R^2 = 0.99$, RMSD ≈ 0.03), demonstrating that the thermal-integration approach reproduces bulk $F^{14}C$ within analytical uncertainty.

3.3 OM molecular fingerprinting across thermal windows

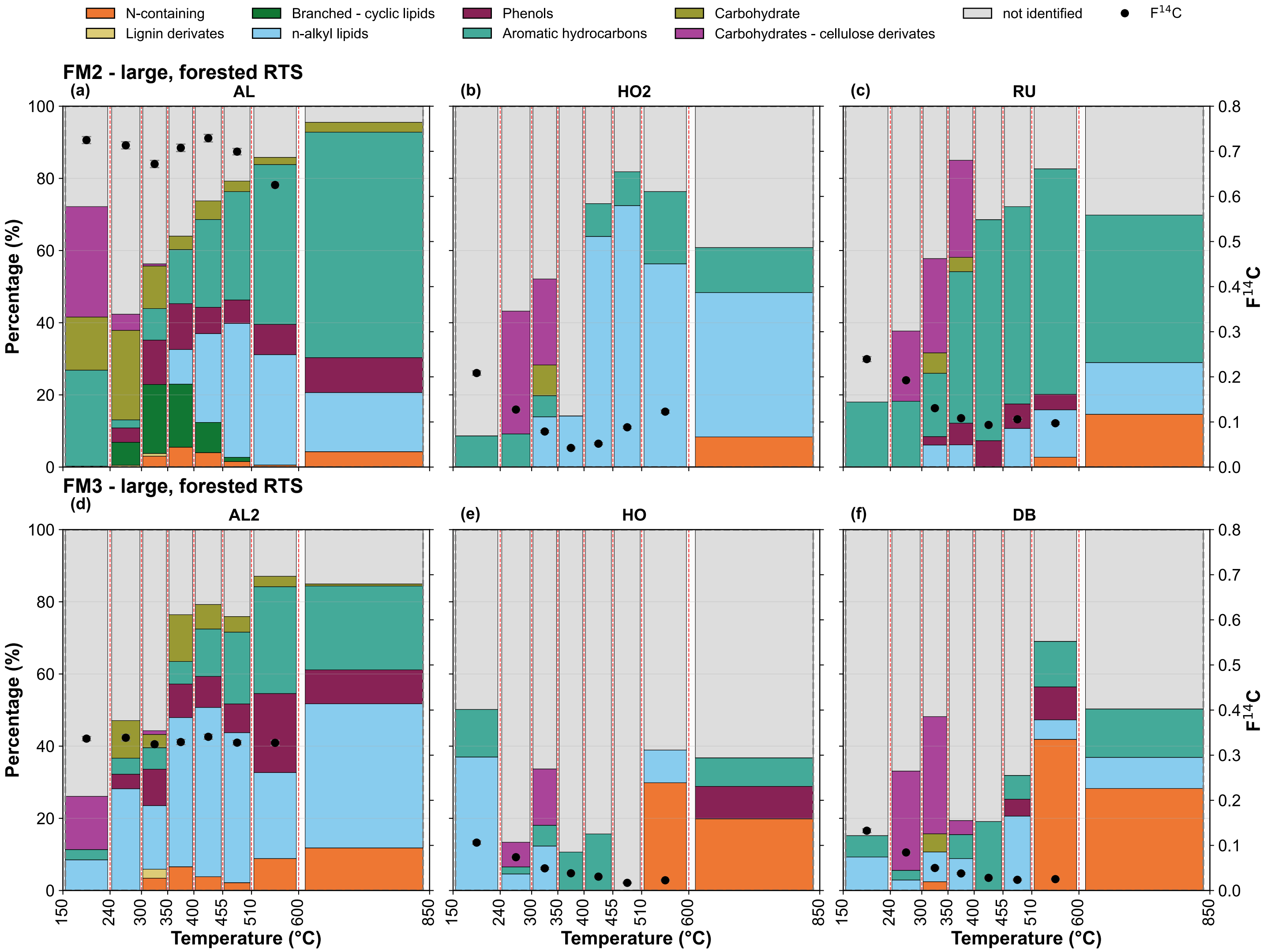

Figure 4. Normalized peak area distributions of molecular compound classes across thermal windows (150–850 °C) for selected thaw slump features (a - c) FM2: active layer (AL), deeper Holocene permafrost (HO2), and runoff (RU). (d - f) FM3: active layer (AL2), Holocene permafrost (HO,) and debris (DB). Compound classes include nitrogen-containing compounds, lignin derivatives, branched–cyclic lipids, n-alkyl lipids, phenols, aromatic hydrocarbons, carbohydrates, and cellulose derivatives, with the $F^{14}C$ fractions measured with ORO on the right.

Interpretable Ts-Py-GCMS chromatograms were obtained for (almost) all thermal windows of AL, HO2 and RU from FM2 and AL2, AL3, HO and DB from FM3 (Fig. 4), whereas other samples (FM2 HO1 and PL, FM3 RU) did not yield usable data due to low signal intensity or excessive noise in most thermal windows (Figs. S15–S16). Compound-class distributions generally reflected a progressive shift from labile, oxygen-rich OM at low temperatures to more compositionally altered, thermally stable material at higher temperatures across all thaw-slump components (peak lists for all analysed samples are provided in Table S4).

In FM2 (Fig. 4a–c), AL, HO2, and RU samples display temperature-dependent shifts in the proportions of specific compound classes. Groups indicating fresh (and potentially bioavailable) OM such as carbohydrates, including cellulose-derived compounds, dominate the 240–300 °C window but are largely absent above 510 °C. Phenols occur across the full thermal range, with variable intensities among geomorphic features, whereas lignin derivatives are detected only in the AL sample. In contrast, proportions of *n*-alkyl lipids and aromatic hydrocarbons increase progressively with temperature, becoming most abundant between 510 and 600 °C. N-containing compounds appear mainly at mid to high temperatures (300–510 °C) and re-emerge in AL and RU in the highest temperature window (600-850 °C. More specifically, the AL sample contains abundant hemicellulose- and cellulose-derived carbohydrates within the 240–300 °C window (e.g., xylose, arabinose, glucose, furfural), followed by phenols 300-350 °C and a distinct shift toward aliphatic lipids and aromatic hydrocarbons between 400 and 510 °C. HO2 contains furfural and branched–cyclic lipids 300-350 °C, transitioning to *n*-alkyl lipids and aromatics in the 510–850 °C range. RU displays methylstyrene compounds at 240–300 °C, cellulose pyrolysis products between 300–350 °C, and increasingly aromatic profiles above 455 °C, with mainly condensed PAHs at 850 °C.

In FM3 (Fig. 4d–f), AL2 (Fig. 4d) and AL3 (Fig. S16) exhibited compound-class distributions broadly consistent with those observed for FM2 AL, with a clear progression from carbohydrates and phenols at lower temperatures to increasing contributions of aliphatic lipids and aromatic compounds at later thermal intervals. Between 350–400 °C, both AL2 and AL3 transitioned toward more thermally stable compounds, with rising proportions of phenols, *n*-alkyl lipids, and aromatics. Above 455 °C, PAHs and N-containing compounds became dominant, particularly in AL3. In contrast, the HO and DB samples (Fig. 4e–f) exhibited an earlier release of hydrocarbons and *n*-alkyl lipids already within the 150–240 °C window. Carbohydrates were largely absent from HO but appeared in DB above 350 °C, while phenols and N-containing compounds were mainly detected at higher temperatures. Chromatograms from the 455–510 °C interval in HO did not yield reliable compound matches. At lower temperatures (240–300 °C), cellulose pyrolysis products (e.g., furfural), methylstyrene compounds, and short- to mid-chain *n*-alkyl lipids occurred across AL2, AL3, HO, and DB. AL2 and AL3 also contained phenols consistent with lignocellulose decomposition. Both HO and DB yielded *n*-aldehydes and levoglucosan, while DB additionally released nonanal and decanal already at 240–300 °C. At the highest temperatures (600–850 °C), persistent compounds included long-chain *n*-alkyl lipids, condensed aromatics (e.g., naphthalene derivatives), and N-containing compounds, representing the residual products of OM decomposition.

https://doi.org/10.5194/egusphere-2026-845
Preprint. Discussion started: 17 February 2026

4 Discussion

4.1 OM stability mechanisms across geomorphic features

Thermal behaviour, radiocarbon patterns, and molecular compositions together show that fundamentally different OM pools are present within the different geomorphic features of the four slumps. Thermograms from FM2 and FM3 demonstrate that AL material begins oxidising at much lopwer temperatures than PF, DB and RU and exhibits a distinct structure, expressed either as a sharp early peak or as a bimodal profile with comparable low- and mid-temperature contributions (Fig. 3a,c). These patterns are consistent with lower mean activation energies in AL samples ($\mu_E \approx$ 152–156 kJ mol^{-1}) and, particularly in FM3, broader activation-energy distributions ($\sigma_E \approx$ 21–24 kJ mol^{-1}), reflecting energetically heterogeneous and comparatively reactive OM pools. In contrast, PF, DB, and RU samples show later onsets of CO_2 release, unimodal peaks centred near ~370–400 °C, and pronounced high-temperature tails characteristic of thermally stable carbon. These features coincide with higher μ_E values ($\approx$ 162–171 kJ mol^{-1}) and consistently elevated but more uniform σ_E values ($\approx$ 17–24 kJ mol^{-1}) across deeper units, indicating a dominance of energetically resistant OM with less variability in stabilisation mechanisms than observed in the AL.

Py-GCMS molecular fingerprints provide a mechanistic explanation for these contrasting thermogram shapes when compared within equivalent thermal windows. In low-temperature windows (240–350 °C), AL samples are relatively enriched in carbohydrate- and cellulose-derived pyrolysates compared to PF, DB, and RU, consistent with the dominance of recently produced, oxygen-rich OM that oxidises early. At higher temperatures (>455 °C), all features show increasing contributions from aromatic hydrocarbons and long-chain n-alkyl lipids; however, these compounds dominate the high-temperature fractions of PF, DB, and RU, whereas AL retains a more mixed molecular signature. This enrichment of condensed and lipid-rich structures in PF-derived material aligns with their broad thermogram peaks and extended high-temperature tails. Similar temperature-dependent compositional shifts have been reported for permafrost OM elsewhere, where aromatic and lipid-rich components control high-temperature reactivity (Tolu et al., 2015; Zaccone et al., 2011). Together, these observations identify the primary molecular divide between biologically active surface horizons and deeper, cryogenically preserved permafrost-derived pools.

Radiocarbon profiles across thermal windows reinforce this interpretation. AL samples in FM2 maintain high $F^{14}C$ values (~0.73–0.63), whereas the FM3 AL samples show lower values (~0.33–0.27), reflecting that AL2 and AL3 were collected from deeper positions within the active layer than the surface AL sampled at FM2, leading to smaller contributions of recent vegetation and instead greater contributions of older, legacy OM. Although AL samples from both RTS do not display strictly invariant $F^{14}C$ values across thermal windows, they show only modest variation relative to PF, DB and RU samples, and several AL fractions as well as the FM2 HO2 sample even show local increases in $F^{14}C$ with increasing temperature, indicating that a small fraction of comparatively young OM persists into higher-temperature (higher-energy) windows. Such complexity suggests that much of the carbon oxidised across low- to mid-temperature windows derives from surface-influenced or recently cycled sources with overlapping activation-energy domains rather than a simple "young = low-T / old = high-T" structure. Also, $F^{14}C$ values are very different between AL samples from FM2 and FM3; this aligns with cryoturbated or compositionally heterogeneous soil horizons within this seasonally thawed layer, where young and older OM can co-occur within similar energetic ranges. In contrast to AL samples, PF, DB and RU display systematic and often steep declines in $F^{14}C$ with increasing temperature, consistent with sequential oxidation of progressively older and more refractory pools.

Activation energy-resolved $F^{14}C$ spectra further reinforce these trends in energy space. AL material retains high to intermediate $F^{14}C$ across low-to-mid E, with only a minor old fraction emerging in the high-E tail. In contrast, PF, DB and RU are uniformly depleted across nearly the entire $p(0,E)$ spectrum, with the strongest depletion at highest E values, indicating that the most oxidation-resistant fractions are also the oldest. FM3 AL horizons show large σ_E values (≈ 21–24 kJ mol^{-1}), reflecting substantial internal heterogeneity due to mixed plant inputs, cryoturbation, and variable degrees of protection. These energetic patterns highlight that OM stability arises from interactions between molecular composition, cryogenic preservation, and physical or mineral protection (Grant et al., 2019; Hemingway et al., 2017, 2019).

Similarly, μ_E vs. bulk $F^{14}C$ relationships reveal clear clustering (Supplementary materials Figs. S17-18). AL samples from both slumps occupy a low μ_E, high $F^{14}C$ domain, whereas PF, DB and RU plot consistently at higher μ_E and lower $F^{14}C$. As expected, these patterns mirror the thermogram shapes and activation-energy spectra: low μ_E values reflect lower kinetic barriers associated with labile or less-protected material, whereas high μ_E values reflect the stronger stabilisation of permafrost-derived pools. AL samples consistently occupy a low- μ_E, high-$F^{14}C$ domain, whereas PF, DB and RU plot toward higher μ_E and lower $F^{14}C$. σ_E patterns follow the same structure: broader distributions in AL, narrower ones in PF-derived material. Exceptions—including the HO2 high-E young fraction and several AL windows containing young OM at higher temperatures—reflect the presence of protected or mineral-associated carbon within active-layer and upper-permafrost horizons.

Across both slumps, $F^{14}C$ decreases systematically with increasing μ_E (Fig. 5a). The corresponding μ_E –ROC/TOC relationship (Fig. S19) shows that these energetic differences are reflected in operational thermal recalcitrance: AL consistently exhibits low ROC/TOC values at low μ_E, whereas PF and mobilised units DB and RU occupy a high-ROC/TOC, high-μ_E field. Importantly, these relationships describe feature-level end-member behaviour rather than within-feature structure. As shown above, individual AL samples can host young and old carbon across overlapping activation-energy ranges, and thus do not follow a strict "young = low-T / old = high-T" rule internally. Instead, the µE–$F^{14}C$ and µE–ROC/TOC trends emerge when contrasting surface versus permafrost-derived pools at the scale of geomorphic units. Together, these trends define two internally coherent stability domains—"young and labile" versus "old and recalcitrant"—within which OM from FM2 and FM3 can be consistently interpreted. Having established these domains for the two fully characterised slumps, we now extend the comparison to all four RTS using the bulk metrics (ROC/TOC and bulk $F^{14}C$) available across sites.

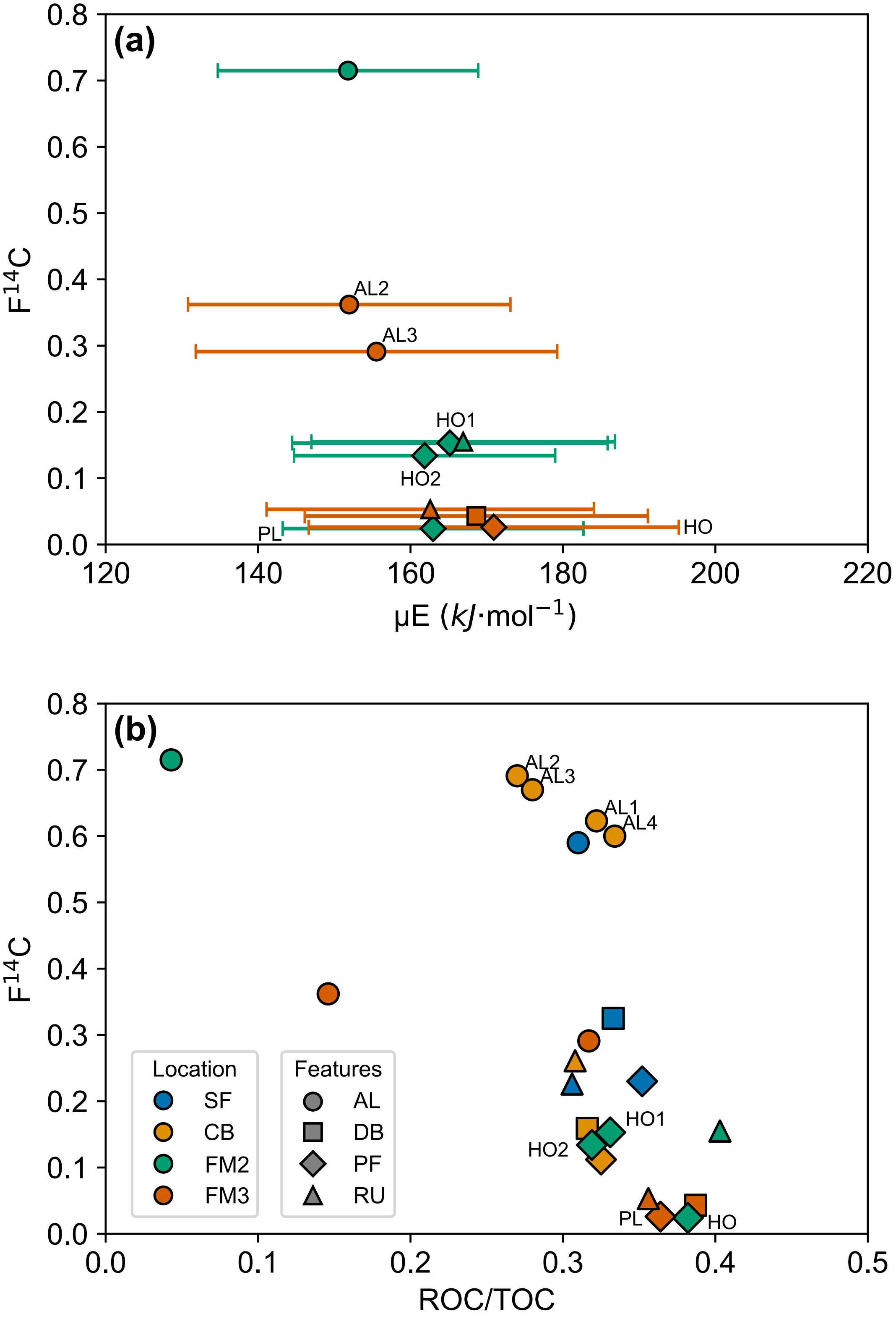
(a)
F14C
0.0
0.1
0.2
0.3
0.4
0.5
0.6
0.7
0.8
AL2
AL3
HO1
HO2
PL
HO
120
140
160
180
200
220
μE (kJ·mol−1)
(b)
F14C
AL2
AL3
AL1
AL4
HO1
HO2
PL
HO
Location
SF
CB
FM2
FM3
Features
AL
DB
PF
RU
0.0
0.1
0.2
0.3
0.4
0.5
ROC/TOC

Figure 5. Panel (a) Relationship between $F^{14}C$ and mean activation energy (μ_E) across thaw slump samples from the Peel Plateau. Horizontal error bars represent the standard deviation (σ_E) of the activation energy distributions, reflecting the energetic heterogeneity of organic matter thermal decomposition. Panel (b) Bulk $F^{14}C$ values (from Bröder et al., 2021) are compared with ROC/TOC ratios from SoliTOC measurements (see definition in the text) across four thaw slump locations and their respective features. Different features are indicated by shapes: circles represent active layer (AL), squares debris (DB), diamonds permafrost (PF), and triangles runoff (RU). Colours correspond to sampling locations: blue for SF, orange for CB, green for FM2, and red for FM3.

4.2 RTS-scale differences in thermal lability and radiocarbon

Across the Peel Plateau sites, ROC/TOC ratios (from SoliTOC analyses) and bulk $F^{14}C$ patterns reveal that slump morphology, vegetation, and active-layer thickness regulate only the surface OM pools, whereas deeper permafrost-derived material remains compositionally and thermally uniform. At the forested slumps FM2 and FM3, AL horizons show higher TOC_{400} and distinct radiocarbon signatures that reflect greater biological inputs and deeper seasonal thaw. FM2 AL is the youngest and most labile, consistent with substantial modern vegetation input. FM3 AL is more heterogeneous because AL2/AL3 samples were collected at greater depths within this cryoturbated layer containing a mix of young and older OM. In contrast, CB and SF—both tundra sites with thin active layers—show lower TOC_{400} but still young bulk $F^{14}C$, indicating low OM input rather than rapid turnover. Despite this ecological variability at the surface, PF, DB, and RU units from all four RTS consistently exhibit higher ROC/TOC and lower bulk $F^{14}C$, showing that the deep, cryogenically preserved, low-OC permafrost substrate mobilised by abrupt thaw and erosion is effectively invariant across the region.

These across-slump differences are most clearly expressed when bulk age and thermal partitioning are combined in ROC/TOC–$F^{14}C$ space (Fig. 5b). AL samples from all RTS plot within a “young, thermally labile” domain, but their position reflects ecological setting: FM2 AL is the youngest and most labile; FM3 AL is moderately depleted and intermediate in stability; and tundra AL (CB/SF) is more thermally resistant yet still young in radiocarbon age owing to limited biological input. In contrast, PF, DB and RU from every slump occupy a compact, old and recalcitrant cluster. This demonstrates that the mechanistic distinctions identified previously are not site-specific: the PF–DB–RU continuum forms a consistent, regionally coherent stability field regardless of vegetation, or slump size. This pattern aligns with prior studies showing that RTS in the Peel Plateau predominantly mobilise radiocarbon-depleted particulate OM from deeper permafrost with limited compositional alteration during initial transport (Bröder et al., 2021; Keskitalo et al., 2021; Shakil et al., 2020; Zolkos et al., 2019).

Overall, RTS-scale contrasts indicate that ecological setting and slump morphology primarily influence the composition and stability of active-layer OM, whereas deeper permafrost-derived pools exhibit consistent thermal and radiocarbon behaviour across all slumps. Importantly, all four RTS display uniformly low TOC in PF (HO and PL), DB and RU units, with no evidence for peat-rich or historically high-productivity ecosystems. This pattern aligns with regional mapping and previous work showing that the Peel Plateau is largely underlain by glacial/moraine-derived, ice-rich sediments rather than organic-rich deposits. The uniformity of PF-derived material across slumps therefore reflects mobilisation of a broadly homogeneous, low-OC, cryogenically preserved substrate, setting the stage for evaluating its regional carbon-cycle significance in the next section.

4.3 RTS carbon in regional and circumpolar context

Distilling the feature-level and RTS-level patterns into a regional perspective shows that slumps on the Peel Plateau primarily mobilise old, thermally stable permafrost-derived carbon, reflecting both their geomorphic configuration and the moraine–till substrate underlying soils of the region. Across FM2, FM3, CB and SF, deeper PF, as well as mobilised components DB and RU consistently share low bulk $F^{14}C$, high ROC/TOC and high μ_E, indicating mobilisation and export of a broadly uniform pool of previously cryogenically preserved, relatively oxidation-resistant OM. These signatures match regional observations that Peel Plateau slumps export particulate OM largely originating from permafrost layers exposed at the headwalls rather than recently produced vegetation or active-layer material (Bröder et al., 2021; Keskitalo et al., 2021; Shakil et al., 2020; Zolkos et al., 2019). Importantly, the uniformly low TOC contents in PF, HO, DB and RU across all slumps further show that neither FM2/FM3 nor CB/SF host significant extents of peat-rich or historically productive ecosystems—consistent with a glacial–moraine, ice-rich substrate.

The stability of the exported OM is further supported by incubation studies from the Peel Plateau and comparable moraine–till permafrost settings elsewhere in the Arctic. Laboratory and field incubations on mineral-rich permafrost soils from north-west Canada, Alaska, and other glaciated terrains demonstrate that respiration-resistant carbon pools are dominated by mineral-associated and physically protected fractions, while only a small labile component is rapidly decomposed following thaw (Estop-Aragonés et al., 2020; Littlefair et al., 2017; Schädel et al., 2014; Vaughn and Torn, 2019). These systems are characterised by relatively low organic-carbon concentrations and strong mineral control on OM stabilisation, closely matching the geomorphic and substrate conditions of the Peel Plateau. The persistence of old, high- μ_E, high-ROC/TOC carbon in PF, DB and RU observed here mirrors these results, indicating that slump processes in this region primarily redistribute protected permafrost material downslope with minimal compositional alteration, rather than triggering substantial early-stage degradation. These findings contrast with observations made for so-called Yedoma permafrost. This late Pleistocene, syngenetic, silt-dominated, ice-rich permafrost contains some of the highest TOC ground-ice contents in the Arctic, storing ~327–466 Gt C globally and representing up to one-third of the deep-frozen carbon pool (Martens et al., 2023; Strauss et al., 2017, 2025). Mapping studies show that the vast majority of Yedoma occurs in North Asia, whereas the Canadian share is small and spatially restricted (Morgenstern et al., 2013; Strauss et al., 2017). This substrate contrast has direct implications for carbon dynamics: erosion of Yedoma deposits can mobilise extremely carbon-rich and comparatively microbially labile organic matter, as shown by incubation and field studies reporting high respiration rates and rapid carbon losses following thaw (Knoblauch et al., 2013; Strauss et al., 2017; Vonk et al., 2013). In contrast, thaw slumps developed in moraine–till

https://doi.org/10.5194/egusphere-2026-845
Preprint. Discussion started: 17 February 2026

terrains mobilise permafrost carbon characterised by low TOC concentrations and strong mineral association, resulting in compositionally uniform, physically protected OM that resists rapid oxidation. Substrate type therefore plays a central role in determining the fate of eroded permafrost OM and must be explicitly considered when extrapolating thaw-slump impacts to the pan-Arctic scale.

5 Conclusions

Across thermal, isotopic, and molecular measurements, our results show that organic-matter stability in Peel Plateau thaw slumps is primarily structured by geomorphic origin and protection state, with a clear contrast between active-layer material and permafrost-derived carbon. The active layer contains younger and more reactive OM influenced by contemporary vegetation inputs, but cryoturbation and increasing sampling depth allow older, legacy carbon to contribute within this horizon. In contrast, permafrost material—and the debris and runoff derived from it—is uniformly radiocarbon-depleted, thermally stable, and compositionally resistant, indicating that debris and runoff largely reflect downslope mobilisation of permafrost-derived OM rather than distinct carbon pools.

Thermal resistance and $F^{14}C$ activity generally covary across these features, but not through a simple ordering of "young = low *E*" and "old = high *E*." Activation energy-resolved $F^{14}C$ spectra and Ts-Py-GCMS compound classes show that young and old fractions can overlap in energetic space due to mineral association, aggregation, and cryogenic preservation. This explains why AL horizons can retain stabilised, higher-energy fractions, and why PF horizons include components of differing energetic stability. Despite this heterogeneity, PF, DB, and RU consistently occupy high-energy, radiocarbon-depleted domains, while AL remains restricted to lower-energy, younger or intermediate-age spaces, confirming that the dominant controls on OM stability lie in source, composition, and degree of protection.

A key outcome is that early-stage RTS mobilisation does not substantially alter the thermal stability or radiocarbon characteristics of PF-derived particulate OM. Instead, slumping primarily redistributes compositionally resistant, ancient carbon downslope with little evidence for rapid transformation, consistent with observations from other mass-wasting–dominated systems. In this study, resistance to degradation is inferred from thermal and isotopic proxies rather than direct measurements of mineralisation, and thus reflects OM persistence rather than instantaneous CO_2 production. These patterns are consistent across all four RTS (FM2, FM3, CB, and SF), despite pronounced ecological differences in active-layer composition. Forested and tundra slumps show contrasting AL properties, but their PF horizons—as well as thaw-eroded debris (DB) and exported runoff material (RU)—are characterised by uniformly old, thermally stable, and low-TOC substrates. This convergence across sites reflects the shared glacial–moraine, ice-rich geological setting of the Peel Plateau. Unlike Yedoma, which consists of thick, syngenetic, ice-rich, and carbon-dense deposits, moraine/till terrains host lower-TOC, cryogenically reworked material with distinct stabilisation histories. RTS developed in such substrates therefore mobilise a fundamentally different permafrost carbon pool than Yedoma-derived slumps, with important implications for how thaw-mobilised carbon is redistributed and for how RTS impacts should—and should not—be generalised across the Arctic.

Predicting the fate of thaw-mobilised permafrost carbon requires integrating OM age, composition, and energetic stability within geomorphic context. By resolving how these properties co-vary across RTS features and across slump types, this study provides a mechanistic basis for understanding why RTS preferentially export long-preserved, protected OM and how these processes shape downstream carbon fluxes in glacial-moraine landscapes. Such structure-informed perspectives are essential for constraining Arctic carbon-cycle feedbacks under continued warming.

5.1.1 Data availability

Additional data are provided in the supplementary material.

5.1.2 Author contributions

LB secured project funding. LB, KK and JV supplied materials and contributed to the description of sample context. MB conducted the majority of measurements, with guidance from NH for the radiocarbon analyses, and performed sample preparation together with NH. TE assisted with Ts-Py-GCMS data interpretation, and JDH provided expertise on the energy distribution analysis. MB led the manuscript writing, with all authors contributing to data interpretation and providing critical feedback on the analysis and manuscript.

5.1.3 Competing interests

The authors declare that they have no conflict of interest.

5.1.4 Acknowledgements:

We thank Thomas Blattmann for laboratory and technical support with the Ts-Py-GCMS analyses; Irene Brunner and Nathalie Dubois for conducting the SoliTOC measurements at EAWAG; and Philip Wenig for providing guidance on OpenChrom use. We are grateful to Sebastian Näher for insightful discussions and suggestions on how to interpret the GC/MS data, and to Urs Ramsperger, Lukas Wacker, and the LIP staff for their assistance with AMS measurements. Special thanks go to Daniele De Maria for his early support in setting up and troubleshooting the DTI interface.

5.1.5 Financial support

This research was funded by the Swiss National Science Foundation (SNF – grant no. 200021-204093 awarded to L.B.). Additional support was provided by the facilities and infrastructure of ETH Zurich, which enabled the analytical and laboratory work presented in this study. K. Keskitalo and J. E. Vonk acknowledge funding from a European Research Council (ERC)

Starting Grant (THAWSOME, grant no. 676982). J. E. Vonk further acknowledges funding from the Nederlandse Organisatie voor Wetenschappelijk Onderzoek (NWO, Dutch Research Council; Rubicon grant no. 019.212EN.033).

5.1.6 Review statement:

This paper was edited by [Editor's Name] and reviewed by [number] anonymous referees. The evaluation process was carried out in the open discussion forum of Biogeosciences.

https://doi.org/10.5194/egusphere-2026-845
Preprint. Discussion started: 17 February 2026

References

Abbott, B. W., Larouche, J. R., Jones, J. B., Bowden, W. B., and Balser, A. W.: Elevated dissolved organic carbon biodegradability from thawing and collapsing permafrost, J. Geophys. Res. Biogeosci., 119, 2049–2063, https://doi.org/10.1002/2014JG002678, 2014.

Bockheim, J. G. and Tarnocai, C.: Recognition of cryoturbation for classifying permafrost-affected soils, Geoderma, 81, 281–293, https://doi.org/10.1016/S0016-7061(97)00115-8, 1998.

Bolandini, M. A., De Maria, D., Haghipour, N., Wacker, L., Hemingway, J. D., Eglinton, T. I., and Bröder, L.: Towards online ramped oxidation (ORO)-AMS for thermal dissection and serial radiocarbon analysis of complex organic matter, Radiocarbon, 1–16, https://doi.org/10.1017/RDC.2025.6, 2025.

Bravo, A. G., Bouchet, S., Tolu, J., Björn, E., Mateos-Rivera, A., and Bertilsson, S.: Molecular composition of organic matter controls methylmercury formation in boreal lakes, Nat. Commun., 8, 1–9, https://doi.org/10.1038/NCOMMS14255, 2017.

Bröder, L., Keskitalo, K. H., Zolkos, S., Shakil, S., Tank, S. E., Kokelj, S. V., Tesi, T., Van Dongen, B. E., Haghipour, N., Eglinton, T. I., and Vonk, J. E.: Preferential export of permafrost-derived organic matter as retrogressive thaw slumping intensifies, Environmental Research Letters, 16, 054059, https://doi.org/10.1088/1748-9326/ABEE4B, 2021.

Derenne, S. and Quéné, K.: Analytical pyrolysis as a tool to probe soil organic matter, J. Anal. Appl. Pyrolysis, 111, 108–120, https://doi.org/10.1016/J.JAAP.2014.12.001, 2015.

Drake, T. W., Wickland, K. P., Spencer, R. G. M., McKnight, D. M., and Striegl, R. G.: Ancient low-molecular-weight organic acids in permafrost fuel rapid carbon dioxide production upon thaw, Proceedings of the National Academy of Sciences, 112, 13946–13951, https://doi.org/10.1073/PNAS.1511705112, 2015.

Estop-Aragonés, C., Olefeldt, D., Abbott, B. W., Chanton, J. P., Czimczik, C. I., Dean, J. F., Egan, J. E., Gandois, L., Garnett, M. H., Hartley, I. P., Hoyt, A., Lupascu, M., Natali, S. M., O'Donnell, J. A., Raymond, P. A., Tanentzap, A. J., Tank, S. E., Schuur, E. A. G., Turetsky, M., and Anthony, K. W.: Assessing the Potential for Mobilization of Old Soil Carbon After Permafrost Thaw: A Synthesis of 14C Measurements From the Northern Permafrost Region, Global Biogeochem. Cycles, 34, e2020GB006672, https://doi.org/10.1029/2020GB006672, 2020.

French, H. M.: The periglacial environment, Wiley, Chichester, UK, 459, 2007.

Grant, K. E., Galy, V., Chadwick, O. A., and Derry, L. A.: Thermal oxidation of carbon in organic matter rich volcanic soils: insights into SOC age differentiation and mineral stabilization, Biogeochemistry, 144, 291–304, https://doi.org/10.1007/S10533-019-00586-1, 2019.

Harris, D., Horwáth, W. R., and van Kessel, C.: Acid fumigation of soils to remove carbonates prior to total organic carbon or CARBON-13 isotopic analysis, Soil Science Society of America Journal, 65, 1853–1856, https://doi.org/10.2136/SSSAJ2001.1853, 2001.

rampedpyrox: open-source tools for thermoanalytical data analysis:

Hemingway, J. D., Rothman, D. H., Rosengard, S. Z., and Galy, V.: Technical note: An inverse method to relate organic carbon reactivity to isotope composition from serial oxidation, Biogeosciences, 14, 5099–5114, https://doi.org/10.5194/BG-14-5099-2017, 2017.

Hemingway, J. D., Rothman, D. H., Grant, K. E., Rosengard, S. Z., Eglinton, T. I., Derry, L. A., and Galy, V.: Mineral protection regulates long-term global preservation of natural organic carbon, Nature, 570, 228–231, https://doi.org/10.1038/s41586-019-1280-6, 2019.

Hugelius, G., Strauss, J., Zubrzycki, S., Harden, J. W., Schuur, E. A. G., Ping, C. L., Schirrmeister, L., Grosse, G., Michaelson, G. J., Koven, C. D., O'Donnell, J. A., Elberling, B., Mishra, U., Camill, P., Yu, Z., Palmtag, J., and Kuhry, P.: Estimated stocks of circumpolar permafrost carbon with quantified uncertainty ranges and identified data gaps, Biogeosciences, 11, 6573–6593, https://doi.org/10.5194/bg-11-6573-2014, 2014.

Kaal, J., Martínez Cortizas, A., and Nierop, K. G. J.: Characterisation of aged charcoal using a coil probe pyrolysis-GC/MS method optimised for black carbon, J. Anal. Appl. Pyrolysis, 85, 408–416, https://doi.org/10.1016/J.JAAP.2008.11.007, 2009.

Kaal, J., Wagner, S., and Jaffé, R.: Molecular properties of ultrafiltered dissolved organic matter and dissolved black carbon in headwater streams as determined by pyrolysis-GC/MS, J. Anal. Appl. Pyrolysis, 118, 181–191, https://doi.org/10.1016/J.JAAP.2016.02.003, 2016.

Keskitalo, K. H., Bröder, L., Shakil, S., Zolkos, S., Tank, S. E., Van Dongen, B. E., Tesi, T., Haghipour, N., Eglinton, T. I., Kokelj, S. V., and Vonk, J. E.: Downstream Evolution of Particulate Organic Matter Composition From Permafrost Thaw Slumps, Front. Earth Sci. (Lausanne)., 9, 642675, https://doi.org/10.3389/feart.2021.642675, 2021.

Knoblauch, C., Beer, C., Sosnin, A., Wagner, D., and Pfeiffer, E. -M.: Predicting long-term carbon mineralization and trace gas production from thawing permafrost of <scp>N</scp> ortheast <scp>S</scp> iberia, Glob. Chang. Biol., 19, 1160–1172, https://doi.org/10.1111/gcb.12116, 2013.

Kokelj, S. V., Lacelle, D., Lantz, T. C., Tunnicliffe, J., Malone, L., Clark, I. D., and Chin, K. S.: Thawing of massive ground ice in mega slumps drives increases in stream sediment and solute flux across a range of watershed scales, J. Geophys. Res. Earth Surf., 118, 681–692, https://doi.org/10.1002/JGRF.20063, 2013.

Kokelj, S. V., Tunnicliffe, J., Lacelle, D., Lantz, T. C., Chin, K. S., and Fraser, R.: Increased precipitation drives mega slump development and destabilization of ice-rich permafrost terrain, northwestern Canada, Glob. Planet. Change, 129, 56–68, https://doi.org/10.1016/J.GLOPLACHA.2015.02.008, 2015.

Kokelj, S. V., Lantz, T. C., Tunnicliffe, J., Segal, R. A., and Lacelle, D.: Climate-driven thaw of permafrost preserved glacial landscapes, northwestern Canada, Geology, 45, 371–374, https://doi.org/10.1130/G38626.1, 2017.

Kokelj, S. V., Kokoszka, J., Van Der Sluijs, J., Rudy, A. C. A., Tunnicliffe, J., Shakil, S., Tank, S. E., and Zolkos, S.: Thaw-driven mass wasting couples slopes with downstream systems, and effects propagate through Arctic drainage networks, Cryosphere, 15, 3059–3081, https://doi.org/10.5194/TC-15-3059-2021, 2021.

Komada, T., Anderson, M. R., and Dorfmeier, C. L.: Carbonate removal from coastal sediments for the determination of organic carbon and its isotopic signatures, δ13C and Δ14C: Comparison of fumigation and direct acidification by hydrochloric acid, Limnol. Oceanogr. Methods, 6, 254–262, https://doi.org/10.4319/LOM.2008.6.254, 2008.

Lacelle, D., Fontaine, M., Pellerin, A., Kokelj, S. V., and Clark, I. D.: Legacy of Holocene Landscape Changes on Soil Biogeochemistry: A Perspective From Paleo-Active Layers in Northwestern Canada, J. Geophys. Res. Biogeosci., 124, 2662–2679, https://doi.org/10.1029/2018JG004916, 2019.

De Leeuw, J. W. and Largeau, C.: A Review of Macromolecular Organic Compounds That Comprise Living Organisms and Their Role in Kerogen, Coal, and Petroleum Formation, Organic Geochemistry: Principles and Applications, 23–72, https://doi.org/10.1007/978-1-4615-2890-6_2, 1993.

Lewis, C. A.: The kinetics of biomarker reactions: implications for the assessment of the thermal maturity of organic matter in sedimentary basins, Organic Geochemistry: Principles and Applications, 491–510, https://doi.org/10.1007/978-1-4615-2890-6_22, 1993.

Lewkowicz, A. G. and Way, R. G.: Extremes of summer climate trigger thousands of thermokarst landslides in a High Arctic environment, Nat. Commun., 10, 1–11, https://doi.org/10.1038/S41467-019-09314-7, 2019.

Littlefair, C. A., Tank, S. E., and Kokelj, S. V.: Retrogressive thaw slumps temper dissolved organic carbon delivery to streams of the Peel Plateau, NWT, Canada, Biogeosciences, 14, 5487–5505, https://doi.org/10.5194/BG-14-5487-2017, 2017.

Mann, P. J., Eglinton, T. I., McIntyre, C. P., Zimov, N., Davydova, A., Vonk, J. E., Holmes, R. M., and Spencer, R. G. M.: Utilization of ancient permafrost carbon in headwaters of Arctic fluvial networks, Nat. Commun., 6, 1–7, https://doi.org/10.1038/NCOMMS8856, 2015.

De Maria, D., Fahrni, S. M., Lozac'h, F., Marvalin, C., Walles, M., Camenisch, G., Wacker, L., and Synal, H. A.: Double Trap Interface: A novel gas interface for high throughput analysis of biomedical samples by AMS, Drug Metab. Pharmacokinet., 39, 100400, https://doi.org/10.1016/J.DMPK.2021.100400, 2021.

Martens, J., Mueller, C. W., Joshi, P., Rosinger, C., Maisch, M., Kappler, A., Bonkowski, M., Schwamborn, G., Schirrmeister, L., and Rethemeyer, J.: Stabilization of mineral-associated organic carbon in Pleistocene permafrost, Nat. Commun., 14, 2120, https://doi.org/10.1038/s41467-023-37766-5, 2023.

Mishra, U., Hugelius, G., Shelef, E., Yang, Y., Strauss, J., Lupachev, A., Harden, J. W., Jastrow, J. D., Ping, C. L., Riley, W. J., Schuur, E. A. G., Matamala, R., Siewert, M., Nave, L. E., Koven, C. D., Fuchs, M., Palmtag, J., Kuhry, P., Treat, C. C., Zubrzycki, S., Hoffman, F. M., Elberling, B., Camill, P., Veremeeva, A., and Orr, A.: Spatial heterogeneity and environmental predictors of permafrost region soil organic carbon stocks, Sci. Adv., 7, 5236–5260, https://doi.org/10.1126/SCIADV.AAZ5236, 2021.

Morgenstern, A., Ulrich, M., Günther, F., Roessler, S., Fedorova, I., Rudaya, N. A., Wetterich, S., Boike, J., and Schirrmeister, L.: Evolution of thermokarst in East Siberian ice-rich permafrost: A case study, Geomorphology, 201, 363–379, https://doi.org/10.1594/PANGAEA.848491, 2013.

Overland, J. E., Dunlea, E., Box, J. E., Corell, R., Forsius, M., Kattsov, V., Olsen, M. S., Pawlak, J., Reiersen, L. O., and Wang, M.: The urgency of Arctic change, Polar Sci., 21, 6–13, https://doi.org/10.1016/J.POLAR.2018.11.008, 2019.

Ping, C. L., Bockheim, J. G., Kimble, J. M., Michaelson, G. J., and Walker, D. A.: Characteristics of cryogenic soils along a latitudinal transect in Arctic Alaska, Journal of Geophysical Research: Atmospheres, 103, 28917–28928, https://doi.org/10.1029/98jd02024, 1998.

Ping, C. L., Michaelson, G. J., Jorgenson, M. T., Kimble, J. M., Epstein, H., Romanovsky, V. E., and Walker, D. A.: High stocks of soil organic carbon in the North American Arctic region, Nat. Geosci., 1, 615–619, https://doi.org/10.1038/ngeo284, 2008.

Ramage, J. L., Irrgang, A. M., Herzschuh, U., Morgenstern, A., Couture, N., and Lantuit, H.: Terrain controls on the occurrence of coastal retrogressive thaw slumps along the Yukon Coast, Canada, J. Geophys. Res. Earth Surf., 122, 1619–1634, https://doi.org/10.1002/2017JF004231, 2017.

Ramsperger, U., De Maria, D., Gautschi, P., Maxeiner, S., Müller, A. M., Synal, H. A., and Wacker, L.: Lea—a novel low energy accelerator for 14C dating, Radiocarbon, 66, 1280–1288, https://doi.org/10.1017/RDC.2023.85, 2024.

Rantanen, M., Karpechko, A. Y., Lipponen, A., Nordling, K., Hyvärinen, O., Ruosteenoja, K., Vihma, T., and Laaksonen, A.: The Arctic has warmed nearly four times faster than the globe since 1979, Commun. Earth Environ., 3, 1–10, https://doi.org/10.1038/s43247-022-00498-3, 2022.

Reimer, P. J., Brown, T. A., and Reimer, R. W.: Discussion: Reporting and Calibration of Post-Bomb 14C Data, Radiocarbon, 46, 1299–1304, https://doi.org/10.1017/S0033822200033154, 2004.

Reimer, P. J., Austin, W. E. N., Bard, E., Bayliss, A., Blackwell, P. G., Bronk Ramsey, C., Butzin, M., Cheng, H., Edwards, R. L., Friedrich, M., Grootes, P. M., Guilderson, T. P., Hajdas, I., Heaton, T. J., Hogg, A. G., Hughen, K. A., Kromer, B., Manning, S. W., Muscheler, R., Palmer, J. G., Pearson, C., Van Der Plicht, J., Reimer, R. W., Richards, D. A., Scott, E. M., Southon, J. R., Turney, C. S. M., Wacker, L., Adolphi, F., Büntgen, U., Capano, M., Fahrni, S. M., Fogtmann-Schulz, A., Friedrich, R., Köhler, P., Kudsk, S., Miyake, F., Olsen, J., Reinig, F., Sakamoto, M., Sookdeo, A., and Talamo, S.: The IntCal20 Northern Hemisphere Radiocarbon Age Calibration Curve (0-55 cal kBP), Radiocarbon, 62, 725–757, https://doi.org/10.1017/RDC.2020.41, 2020.

Schädel, C., Schuur, E. A. G., Bracho, R., Elberling, B., Knoblauch, C., Lee, H., Luo, Y., Shaver, G. R., and Turetsky, M. R.: Circumpolar assessment of permafrost C quality and its vulnerability over time using long-term incubation data, Glob. Chang. Biol., 20, 641–652, https://doi.org/10.1111/GCB.12417, 2014.

Schnitzer, M. and Monreal, C. M.: Quo Vadis Soil Organic Matter Research? A Biological Link to the Chemistry of Humification, Advances in Agronomy, 113, 143–217, https://doi.org/10.1016/B978-0-12-386473-4.00003-8, 2011.

Schuur, E. A. G., Bockheim, J. G., Canadell, J. G., Euskirchen, E., Field, C. B., Goryachkin, S. V., Hagemann, S., Kuhry, P., Lafleur, P. M., Lee, H., Mazhitova, G., Nelson, F. E., Rinke, A., Romanovsky, V. E., Shiklomanov, N., Tarnocai, C., Venevsky, S., Vogel, J. G., and Zimov, S. A.: Vulnerability of Permafrost Carbon to Climate Change: Implications for the Global Carbon Cycle, Bioscience, 58, 701–714, https://doi.org/10.1641/B580807, 2008.

Schuur, E. A. G., McGuire, A. D., Schädel, C., Grosse, G., Harden, J. W., Hayes, D. J., Hugelius, G., Koven, C. D., Kuhry, P., Lawrence, D. M., Natali, S. M., Olefeldt, D., Romanovsky, V. E., Schaefer, K., Turetsky, M. R., Treat, C. C., and Vonk, J. E.: Climate change and the permafrost carbon feedback, Nature, 520, 171–179, https://doi.org/10.1038/nature14338, 2015.

Segal, R. A., Lantz, T. C., and Kokelj, S. V.: Acceleration of thaw slump activity in glaciated landscapes of the Western Canadian Arctic, Environmental Research Letters, 11, 034025, https://doi.org/10.1088/1748-9326/11/3/034025, 2016a.

Segal, R. A., Lantz, T. C., and Kokelj, S. V.: Acceleration of thaw slump activity in glaciated landscapes of the Western Canadian Arctic, Environmental Research Letters, 11, 034025, https://doi.org/10.1088/1748-9326/11/3/034025, 2016b.

Shakil, S., Tank, S. E., Kokelj, S. V., Vonk, J. E., and Zolkos, S.: Particulate dominance of organic carbon mobilization from thaw slumps on the Peel Plateau, NT: Quantification and implications for stream systems and permafrost carbon release, Environmental Research Letters, 15, 114019, https://doi.org/10.1088/1748-9326/ABAC36, 2020.

Shakil, S., Tank, S. E., Vonk, J. E., and Zolkos, S.: Low biodegradability of particulate organic carbon mobilized from thaw slumps on the Peel Plateau, NT, and possible chemosynthesis and sorption effects, Biogeosciences, 19, 1871–1890, https://doi.org/10.5194/BG-19-1871-2022, 2022.

Strauss, J., Schirrmeister, L., Grosse, G., Fortier, D., Hugelius, G., Knoblauch, C., Romanovsky, V., Schädel, C., Schneider von Deimling, T., Schuur, E. A. G., Shmelev, D., Ulrich, M., and Veremeeva, A.: Deep Yedoma permafrost: A synthesis of depositional characteristics and carbon vulnerability, Earth. Sci. Rev., 172, 75–86, https://doi.org/10.1016/J.EARSCIREV.2017.07.007, 2017.

Strauss, J., Fuchs, M., Hugelius, G., Miesner, F., Nitze, I., Opfergelt, S., Schuur, E., Treat, C. C., Turetsky, M., Yang, Y., and Grosse, G.: Organic matter storage and vulnerability in the permafrost domain, Encyclopedia of Quaternary Science, 399–410, https://doi.org/10.1016/B978-0-323-99931-1.00164-1, 2025.

Stuiver, M. and Polach, H. A.: Discussion Reporting of 14C Data, Radiocarbon, 19, 355–363, https://doi.org/10.1017/S0033822200003672, 1977.

Synal, H. A., Stocker, M., and Suter, M.: MICADAS: a new compact radiocarbon AMS system, Nucl. Instrum. Methods Phys. Res. B, 259, 7–13, https://doi.org/10.1016/j.nimb.2007.01.138, 2007.

Thomas, M., Monhonval, A., Hirst, C., Bröder, L., Zolkos, S., Vonk, J. E., Tank, S. E., Keskitalo, K. H., Shakil, S., Kokelj, S. V., van der Sluijs, J., and Opfergelt, S.: Evidence for preservation of organic carbon interacting with iron in material displaced from retrogressive thaw slumps: Case study in Peel Plateau, western Canadian Arctic, Geoderma, 433, 116443, https://doi.org/10.1016/J.GEODERMA.2023.116443, 2023.

Tolu, J., Gerber, L., Boily, J. F., and Bindler, R.: High-throughput characterization of sediment organic matter by pyrolysis–gas chromatography/mass spectrometry and multivariate curve resolution: A promising analytical tool in (paleo)limnology, Anal. Chim. Acta, 880, 93–102, https://doi.org/10.1016/J.ACA.2015.03.043, 2015.

Vaughn, L. J. S. and Torn, M. S.: 14C evidence that millennial and fast-cycling soil carbon are equally sensitive to warming, Nat. Clim. Chang., 9, 467–471, https://doi.org/10.1038/s41558-019-0468-y, 2019.

Vonk, J. E., Mann, P. J., Davydov, S., Davydova, A., Spencer, R. G. M., Schade, J., Sobczak, W. V., Zimov, N., Zimov, S., Bulygina, E., Eglinton, T. I., and Holmes, R. M.: High biolability of ancient permafrost carbon upon thaw, Geophys. Res. Lett., 40, 2689–2693, https://doi.org/10.1002/grl.50348, 2013.

Vonk, J. E., Giosan, L., Blusztajn, J., Montlucon, D., Graf Pannatier, E., McIntyre, C., Wacker, L., Macdonald, R. W., Yunker, M. B., and Eglinton, T. I.: Spatial variations in geochemical characteristics of the modern Mackenzie Delta sedimentary system, Geochim. Cosmochim. Acta, 171, 100–120, https://doi.org/10.1016/J.GCA.2015.08.005, 2015.

Wenig, P. and Odermatt, J.: OpenChrom: A cross-platform open source software for the mass spectrometric analysis of chromatographic data, BMC Bioinformatics, 11, 1–9, https://doi.org/10.1186/1471-2105-11-405, 2010.

Zaccone, C., Sanei, H., Outridge, P. M., and Miano, T. M.: Studying the humification degree and evolution of peat down a Holocene bog profile (Inuvik, NW Canada): A petrological and chemical perspective, Org. Geochem., 42, 399–408, https://doi.org/10.1016/j.orggeochem.2011.02.004, 2011.

Zolkos, S., Tank, S. E., and Kokelj, S. V.: Mineral Weathering and the Permafrost Carbon-Climate Feedback, Geophys. Res. Lett., 45, 9623–9632, https://doi.org/10.1029/2018GL078748, 2018.

Zolkos, S., Tank, S. E., Striegl, R. G., and Kokelj, S. V.: Thermokarst Effects on Carbon Dioxide and Methane Fluxes in Streams on the Peel Plateau (NWT, Canada), J. Geophys. Res. Biogeosci., 124, 1781–1798, https://doi.org/10.1029/2019JG005038, 2019.